








# Anisotropic in-plane dielectric and ferroelectric properties of tensile-strained BaTiO<sub>3</sub> films with three different crystallographic orientations

Cite as: AIP Advances **11**, 025016 (2021); <https://doi.org/10.1063/5.0035644>

Submitted: 30 October 2020 . Accepted: 04 January 2021 . Published Online: 09 February 2021

 Trygve M. Raeder,  Theodor S. Holstad,  Inger-Emma Nylund,  Mari-Ann Einarsrud,  Julia Glaum,  Dennis Meier, and  Tor Grande

## COLLECTIONS

Paper published as part of the special topic on [Chemical Physics](#), [Energy, Fluids and Plasmas](#), [Materials Science](#) and [Mathematical Physics](#)

 This paper was selected as an Editor's Pick



View Online



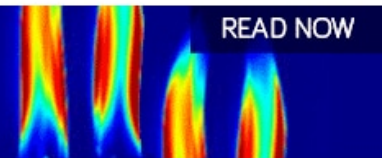
Export Citation



CrossMark

AIP Advances  
Fluids and Plasmas Collection

READ NOW



# Anisotropic in-plane dielectric and ferroelectric properties of tensile-strained BaTiO<sub>3</sub> films with three different crystallographic orientations

Cite as: AIP Advances 11, 025016 (2021); doi: 10.1063/5.0035644

Submitted: 30 October 2020 • Accepted: 4 January 2021 •

Published Online: 9 February 2021



Trygve M. Raeder,  Theodor S. Holstad,  Inger-Emma Nylund,  Mari-Ann Einarsrud,  Julia Glaum,   
Dennis Meier,  and Tor Grande<sup>a)</sup> 

## AFFILIATIONS

Department of Materials Science and Engineering, NTNU Norwegian University of Science and Technology, NO-7491 Trondheim, Norway

<sup>a)</sup> Author to whom correspondence should be addressed: [grande@ntnu.no](mailto:grande@ntnu.no)

## ABSTRACT

Ferroelectric properties of films can be tailored by strain engineering, but a wider space for property engineering can be opened by including crystal anisotropy. Here, we demonstrate a huge anisotropy in the dielectric and ferroelectric properties of BaTiO<sub>3</sub> films. Epitaxial BaTiO<sub>3</sub> films deposited on (100), (110), and (111) SrTiO<sub>3</sub> substrates were fabricated by chemical solution deposition. The films were tensile-strained due to thermal strain confirmed by the enhanced Curie temperature. A massive anisotropy in the dielectric constant, dielectric tunability, and ferroelectric hysteresis loops was observed depending on the in-plane direction probed and the orientation of the films. The anisotropy was low for (111) BaTiO<sub>3</sub>, while the anisotropy was particularly strong for (110) BaTiO<sub>3</sub>, reflecting the low in-plane rotational symmetry. The anisotropy also manifested at the level of the ferroelectric domain patterns in the films, providing a microscopic explanation for the macroscopic response. This study demonstrates that the properties of ferroelectric films can be tailored not only by strain but also by crystal orientation. This is particularly interesting for multilayer stacks where the strain state is defined by the boundary conditions. We propose that other materials can be engineered in a similar manner by utilizing crystal anisotropy.

© 2021 Author(s). All article content, except where otherwise noted, is licensed under a Creative Commons Attribution (CC BY) license (<http://creativecommons.org/licenses/by/4.0/>). <https://doi.org/10.1063/5.0035644>

## INTRODUCTION

There has been great interest devoted to strain engineering for improved ferroelectric properties of thin films.<sup>1-3</sup> In particular, strain engineering has been shown to increase the Curie temperature and remnant polarization<sup>4</sup> and even induce ferroelectricity in otherwise centrosymmetric systems such as SrTiO<sub>3</sub> (STO).<sup>5</sup> These effects were first predicted by theory<sup>6,7</sup> and later confirmed by experiments.<sup>3</sup> For the prototype ferroelectric perovskites PbZr<sub>x</sub>Ti<sub>1-x</sub>O<sub>3</sub> and BaTiO<sub>3</sub> (BTO),<sup>2</sup> compressive strain favors out-of-plane polarization, while tensile strain favors in-plane polarization.<sup>7-11</sup> BTO under tensile strain is the focus of this study, induced by thermal mismatch in the thermal expansion of the BTO film and the STO substrate.<sup>12</sup> The polarization and dielectric constant depend on the strain state, but also on the direction probed and the film orientation. Varying properties may therefore be found in a single strain state

by using different film orientations and measurement directions. Furthermore, the properties and anisotropy of strained films with different orientations will correlate with the ferroelectric domain pattern, providing an additional handle to control the ferroelectric behavior at the local scale. An  $a_1/a_2$  domain pattern, for example, was predicted under tensile strain in (100) BTO with the polarization along the [010] crystallographic axis for the  $a_1$  domain and [001] for the  $a_2$  domain.<sup>8</sup> Likewise, (110) BTO under tensile strain was proposed to possess pure in-plane polarization with components along the in-plane [1-10] and [00-1] directions.<sup>13,14</sup> For (111) BTO on the other hand, a significant out-of-plane component was predicted even at a high tensile strain, in combination with in-plane polarization along the [11-2] direction.<sup>14</sup> The low-symmetry phases of strained (110) and (111) BTO are associated with the enhanced dielectric and ferroelectric properties. Up to now, however, experimental validation of the theoretically predicted domain states has

been virtually non-existent, and to what extent crystal anisotropy can be utilized to engineer the dielectric/ferroelectric properties in strained films remains to be demonstrated.

Here, we report on the anisotropic in-plane ferroelectric and dielectric properties of BTO films grown on (100), (110), and (111) STO substrates. Significant in-plane anisotropy is anticipated in epitaxial BTO films as the polarization is predicted to align with specific crystallographic axes.<sup>7–14</sup> The anisotropy depends on the in-plane rotational symmetry, which is four-, two-, and six-fold when projected into the plane for (100), (110), and (111) orientations, respectively (see Fig. S1.5 of the [supplementary material](#)). The films were fabricated by aqueous chemical solution deposition (CSD),<sup>12</sup> and the in-plane properties of the films were determined using interdigitated electrodes (IDE). High remnant polarization and dielectric tunability were observed for all orientations, and the in-plane anisotropy was particularly high for the (110) oriented BTO film, which correlates with the low in-plane rotational symmetry. We demonstrate that the in-plane ferroelectric and dielectric properties can be fine-tuned and optimized by choosing distinct crystallographic orientations.

## EXPERIMENTAL

BTO thin films were prepared by chemical solution deposition using a pH neutral aqueous route based on the cation precursors  $\text{Ba}(\text{NO}_3)_2$  and Ti-isopropoxide described elsewhere.<sup>12</sup> Ethylenediaminetetraacetic acid (EDTA) and citric acid were used as complexing agents, and ammonia solution was used to increase the pH. All chemicals were obtained from Sigma-Aldrich St. Louis, MI, USA. The solution was adjusted to a concentration of 0.13M and was spin coated onto substrates (Crystal GmbH, Berlin, Germany) at 3000 rpm in a cleanroom (NTNU Nanolab). Each layer was heat treated with a heating rate of  $100^\circ\text{C min}^{-1}$  from ambient temperature to  $450^\circ\text{C}$  at  $50^\circ\text{C min}^{-1}$  up to  $550^\circ\text{C}$  and  $20^\circ\text{C s}^{-1}$  up to  $1000^\circ\text{C}$  in a rapid thermal processing unit (Jipelec JetFirst 200, Semco Technologies, France) with a hold time of 5 min at  $1000^\circ\text{C}$ . This process was repeated eight times to reach the desired thickness.

Interdigitated electrodes (IDEs) were deposited using a lift-off process described in a previous report,<sup>12</sup> with a ma-N 440 negative photoresist (Micro Resist Technology GmbH, Berlin, Germany) exposed using custom design (MLA-150 maskless aligner, Heidelberg, Germany) and developed with a ma-D 332/S developer (Micro Resist Technology GmbH). The electrodes were made by depositing Ti (5 nm) and Pt (20 nm) by e-beam evaporation (ATC series, AJA international, Scituate, MA, United States). Each set of electrodes consisted of 100 fingers with a finger overlap length of  $900\ \mu\text{m}$ . The fingers were designed to be  $2\ \mu\text{m}$  wide with  $8\ \mu\text{m}$  spacing. Accurate dimensions of individual sets of IDEs were measured by an automated image processing tool based on optical micrographs developed internally. The image processing tool was calibrated based on the images from scanning electron microscopy. Dimensions of the individual sets of IDEs can be found in Sec. 6 of the [supplementary material](#).

X-ray diffraction was performed with a diffractometer (Panalytical Empyrean) with a 2D detector and a 4xGe220 monochromator. The films were aligned using the reflections of the  $\text{SrTiO}_3$  substrate, and a 4 h scan time was used to obtain each

reciprocal space map. The uncertainty in the lattice parameters was based on the FWHM of the reflections shown in Figs. S1.1–S1.4 of the [supplementary material](#) when projected onto the corresponding axis.

The TEM lamellas were made using a FEI Helios G4 UX focused ion beam with a EasyLift EX NanoManipulator (Thermo Fisher Scientific, Waltham, MA, USA), and TEM was performed on a Jeol JEM ARM200F cold FEG microscope (Jeol, Tokyo, Japan).

Resonant PFM images were measured using a Cypher S (Oxford Instruments, Abingdon, UK). Vector PFM was performed on an NT-MDT NTEGRA (NT-MDT Spectrum Instruments, Moscow, Russia). An aixACCT TF analyzer 2000 (aixACCT Systems GmbH, Aachen, Germany) with a thin film sample holder was used for electrical characterization, and the electric field was calculated by dividing the voltage by the effective electrode spacing  $a' = a + 4\ln(2)t/\pi$ , as described in Ref. 15, where  $a$  is the actual electrode spacing and  $t$  is the film thickness. The remnant polarization was determined from where the hysteresis loop intersects the y-axis in the first quadrant of the plot, and the coercive field was found from the maximum in the switching current. The capacitive contribution of the substrate was subtracted from the charge collected at the electrodes in order to calculate the polarization in the film. This operation was performed using the model described in Ref. 16. The capacitance was measured at 1 kHz with a small signal voltage of  $0.2\ \text{kV cm}^{-1}$ , and the bias voltage was cycled at 0.1 Hz. The dielectric constant of the films was found by comparing the experimental data to the model described in Ref. 16 and varying the dielectric constant of the film in the model so that the capacitance matched the experimental data. The thickness of the films, the dimensions of the IDEs, and a relative dielectric constant of the STO substrates were used here. The as-recorded data are shown in Sec. 6 of the [supplementary material](#). The temperature-dependence of the dielectric constant of the STO substrates was measured using IDEs on a clean substrate, and the measured dielectric constant as a function of temperature is included in Sec. 7 of the [supplementary material](#). The dielectric constant of the STO substrates at room temperature was 317, as previously reported.<sup>16</sup> The tunability of the dielectric constant is defined as  $(1 - \epsilon_{\min})/\epsilon_{\max}$ , while the unipolar tunability is defined as  $(1 - \epsilon_{\min})/\epsilon_{E=0}$ .

## RESULTS

### Relationship between orientation and structure

BTO films were successfully deposited on (100), (110), and (111) STO substrates by CSD. Bragg–Brentano x-ray diffractograms of the BTO films are shown in Fig. S1.1 of the [supplementary material](#). All three films were single-phase epitaxial BTO following the orientation of the STO substrates. Based on the TEM micrographs (Figs. S2.1 and S2.3), the thicknesses of the (100), (110), and (111) BTO films were determined to be  $230 \pm 4$ ,  $218 \pm 2$ , and  $220 \pm 27\ \text{nm}$ , respectively. The surface topographies of the films are shown in Figs. S3.1, S3.4, and S3.7, and the surface root mean square roughness was about  $2\ \text{nm}$ – $3\ \text{nm}$  for (100) and (110) and  $15.0\ \text{nm}$  for (111) oriented films. The film thicknesses are by far thicker than the critical thickness of  $\sim 5\ \text{nm}$  for BTO on STO for the formation of dislocations at the STO–BTO interface,<sup>17</sup> and potential strain due to the lattice mismatch between STO and BTO is thereby relaxed.

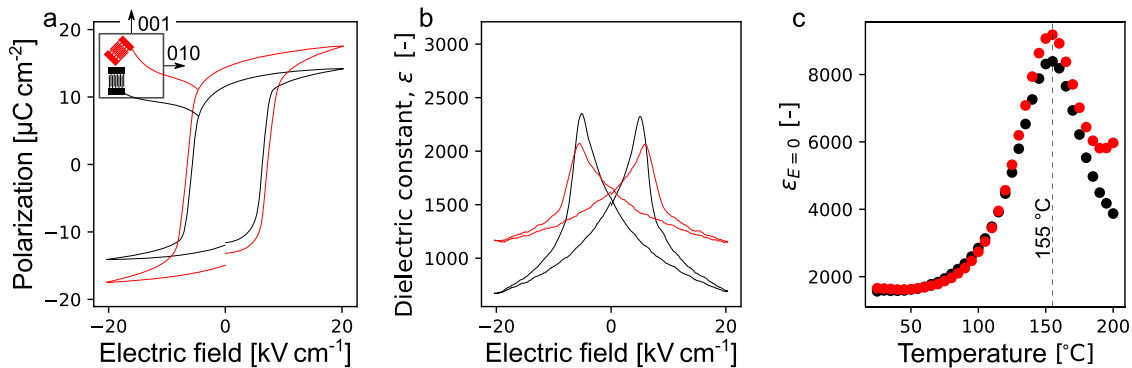


**FIG. 1.** (a) Ferroelectric hysteresis loops (1 Hz) of the (100) BTO film measured with the electric field in-plane along the [0-11] and [001] directions of the STO substrate. (b)  $\epsilon$ - $E$  loops of the dielectric constant (1 kHz) on the (100) BTO film along the same orientations as in (a). (c) The dielectric constant (1 kHz) of the (100) BTO film as a function of temperature at zero bias field.

Reciprocal space maps of the (100) BTO film were obtained near the (310) and (311) reflections (Fig. S1.2). Pseudo-cubic indices are used for the BTO film for simplicity. The average in-plane lattice parameter was found to be  $4.010 \pm 0.023$  Å, which is larger than the average out-of-plane lattice parameter ( $4.000 \pm 0.007$  Å), indicating bi-axial tensile strain.<sup>18</sup> The tensile strain is caused by the thermal strain induced during cooling due to the mismatch in thermal expansion between the film and the substrate.<sup>12</sup> Corresponding reciprocal space maps of the (222) and (310) reflections for (110) BTO and the (312) and (330) reflections for (111) BTO are shown in Figs. S1.3 and S1.4. The lattice parameters are summarized in Fig. S1.5 (see also Table S1.1 for a summary), where the orientation and projection of the pseudo cubic unit cell for the three cases are illustrated. When comparing the in-plane lattice parameters (Fig. S1.5), it is evident that the three films have comparable in-plane tensile strain, which allows for the investigation of the additional impact of the orientational state.

### The (001) oriented BTO film

Different IDEs were deposited, which apply the electric field along the [010], [0-11], and [001] in-plane directions of the (100) oriented BTO film. The ferroelectric polarization-electric field hysteresis loops measured along the [010] and [0-11] directions are illustrated in the inset of Fig. 1(a) ([001] is symmetry equivalent to the [010] direction and therefore leads to identical results). The remnant polarization is anisotropic, being significantly larger along the [0-11] direction ( $P_{0-11} = 14.4 \mu\text{C cm}^{-2}$ ) than along the [001] direction ( $P_{001} = 11.6 \mu\text{C cm}^{-2}$ ). These values are about half the polarization reported for single crystal BTO ( $27 \mu\text{C cm}^{-2}$ ).<sup>19</sup> The same anisotropy was also observed for the coercive field, with  $6.82 \text{ kV cm}^{-1}$  and  $6.22 \text{ kV cm}^{-1}$  for the [0-11] and [001] directions, respectively. The corresponding electric field dependence of the dielectric constants ( $\epsilon$ - $E$  loops) of the (100) BTO film along the two crystallographic directions is shown in Fig. 1(b). The two in-plane directions display comparable dielectric constants at zero field,

**TABLE I.** The coercive field, remnant polarization, full width at half maximum (FWHM) of the switching current, dielectric constant ( $\epsilon$ ), tunability of the dielectric constant, and unipolar tunability of the dielectric constant for the various BTO films and electrode orientations. The maximum and minimum values of each category are given in bold and cursive numbers, respectively (multiple values are highlighted if the difference between each is less than 1%).

Film	$\hat{E}$	Coercive field (kV cm <sup>-1</sup> )	Remnant polarization n (μC cm <sup>-2</sup> )	FWHM (kV cm <sup>-1</sup> )	$\epsilon_{E=0}$ [-]	Tunability of $\epsilon$ (%)	Unipolar tunability of $\epsilon$ (%)	Curie temperature (°C)
(100)	[010]	6.21	11.6	<b>2.03</b>	1501	71.1	56.6	155
	[0-11]	6.81	14.4	2.64	1590	<b>44.5</b>	<b>30.9</b>	155
(110)	Diagonal	6.82	14.4	2.85	1680	56.4	40.0	160
	[1-10]	6.00	16.8	2.96	<b>1396</b>	66.9	48.5	160
	[00-1]	<b>4.46</b>	<b>8.4</b>	3.67	2313	71.3	61.4	155
(111)	[11-2]	5.52	12.1	2.74	2265	61.7	48.2	155
	[-110]	5.56	10.8	3.18	2331	59.0	46.8	155
	Diagonal	5.46	10.5	3.16	2316	57.0	44.6	155

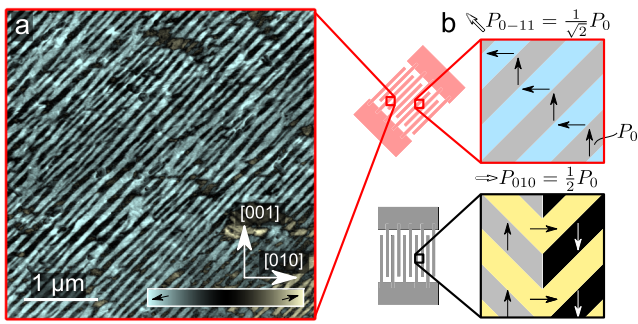


**FIG. 2.** (a) In-plane domain pattern of the poled (100) BTO film between the electrodes oriented with the electric field in the [0-11] direction obtained by resonant PFM (see the Experimental section for details and Sec. 3 of the [supplementary material](#) for the corresponding vector PFM scans). A stripe-like domain configuration with domain walls predominantly oriented along the [011] direction is evident. (b) Schematic illustration of the domain patterns for the two IDE orientations after poling with average polarization along the [0-11] and [010] directions based on our vector PFM data. The magnitude of the average polarization is shown as a fraction of the polarization in a single domain ( $P_0$ ).

and the values are within the range reported for bulk BTO ( $\sim 200$  along the  $c$  axis and  $\sim 4600$  along the  $a$  axis<sup>20</sup>) under ambient conditions. However, large in-plane anisotropy in the tunability, corresponding to the ratio between the maximum and minimum dielectric constant, can be observed in Fig. 1(b). The tunability is higher along the [010] direction compared to the [0-11] direction. The electrical properties of the (100) BTO film are summarized in Table I. The dielectric constant of the (100) BTO film at zero field is shown as a function of temperature in Fig. 1(c) for both orientations of the IDEs. The enhanced Curie temperature reported previously for BTO films prepared by this method is confirmed<sup>12</sup> and demonstrates a maximum in the capacitance at  $155 \pm 5^\circ\text{C}$  for both orientations of the IDEs. The low anisotropy in the dielectric constant persisted for all temperatures up to  $T_C$ . Above the Curie temperature, the anisotropy seemingly increased. This is, however, an artifact caused by the increased leakage current for the electrodes with the electric field oriented along the [0-11] direction, possibly related to surface current (see loss tangent shown in Fig. S4.1).

The full width at half maximum (FWHM) of the switching current (see also Fig. S41) and the unipolar tunability of the dielectric constant are also included in Table I. The unipolar tunability is included because it is relevant for applications where back-switching is undesirable. An expanded version of Table I, including the tunability of the capacitance, is given in Sec. 5 of the [supplementary material](#).

The maximum in-plane polarization in the (100) BTO film was found along the same direction as the maximum in-plane dielectric constant. This is different from single crystal BTO, where the maximum dielectric constant was found orthogonal to the polarization in the tetragonal, the orthorhombic, and the rhombohedral phases. At its roots, such differences in the macroscopic ferroelectric properties usually correspond to differences in the domain pattern, which was investigated by piezoresponse force microscopy (PFM). The characteristic domain pattern recorded after poling the (100) BTO film along the [01-1] direction is shown in the PFM scan image in Fig. 2(a). A pronounced PFM contrast indicates the presence of two domain states, forming a stripe-like pattern with domain walls predominantly oriented along the [011] direction. This observation is consistent with the previous spatially resolved measurements on BTO grown by PLD on NdScO<sub>3</sub> substrates<sup>21,22</sup> and the prediction of  $a_1/a_2$  or  $ca_1/ca_2$  domain patterns in (100) BTO thin films under tensile strain.<sup>8</sup> While comprehensive vector PFM measurements confirm the  $a_1/a_2$  domain configuration, no additional contrast associated with a  $c$ -component was resolved (see Sec. 3 of the [supplementary material](#)). This leads us to the conclusion that, depending on the orientation of the IDE, the poled (100) BTO film exhibited different  $a_1/a_2$  domain configurations between the electrodes. The domain patterns and average polarization values for (100) BTO poled along the [0-11] and [010] directions are sketched in Fig. 2(b).

### The (110) oriented BTO film

The hysteresis loops measured along three crystallographic directions of the BTO films deposited on (110) STO are shown in Fig. 3(a). IDEs were deposited with three different orientations, that is, parallel to the two edges of the sample and at  $45^\circ$ , as illustrated in the inset of Fig. 3(a). These are the same three directions

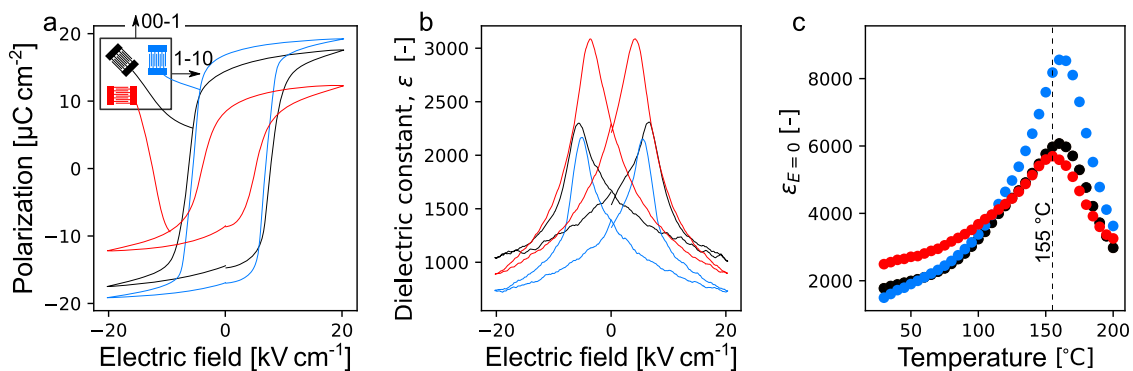


**FIG. 3.** (a) Ferroelectric hysteresis loops (1 Hz) of the (110) BTO film measured with the electric field in the indicated directions of the STO substrate. (b)  $\epsilon$ - $E$  loops of the dielectric constant (1 kHz) for the same electrodes. (c) The dielectric constant (1 kHz) of the film as a function of temperature at zero bias field.

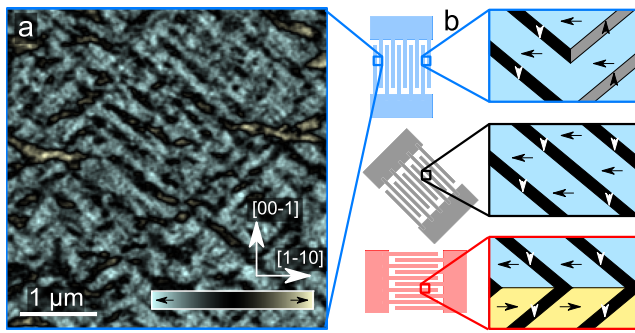


**FIG. 4.** (a) In-plane domain pattern of the poled (110) BTO film recorded by phase calibrated PFM between the electrodes oriented with the electric field in the [1-10] direction. (b) Schematic illustration of the domain pattern for the three IDE orientations (blue, gray, and red) based on the vector PFM measurements. Arrows give the direction of the polarization in the domains.

used for the (100) BTO film, but since (110) BTO has a lower in-plane rotational symmetry [see Fig. S1.5 (b)], the directions are now symmetry inequivalent. The observed in-plane ferroelectric behavior demonstrated a more pronounced anisotropy than in the (100) BTO film, with the maximum remnant polarization along the [1-10] direction and minimum along the [00-1] direction. A corresponding anisotropy in the coercive field is also evident.

The corresponding  $\epsilon$ - $E$  loops of the (110) BTO film are shown in Fig. 3(b) for the three IDE orientations. Strong anisotropy was demonstrated in both the dielectric constant at zero field and in the tunability of the dielectric constant. Notably, the dielectric constant and tunability are much higher when the electric field is oriented along the [00-1] direction. The electrical properties of the (110) BTO film are summarized in Table I. The temperature dependence of the dielectric constant (1 kHz) at zero field along the three directions is shown in Fig. 3(c). A peak in capacitance was observed at  $155 \pm 5^\circ\text{C}$  for the electrodes with the electric field along the [00-1] direction, while a higher Curie temperature ( $160 \pm 5^\circ\text{C}$ ) was observed for the other two orientations.

To investigate the microscopic origin of the pronounced anisotropy, PFM scans were performed on the (110) BTO film. An

in-plane PFM image obtained after poling the (110) BTO film along the [1-10] direction is presented in Fig. 4(a). The domain structure is qualitatively different from the domain pattern in (100) BTO [Fig. 2(a)], showing two preferred orientation directions for the ferroelectric domain walls, both at  $\sim 41^\circ$  with respect to the [1-10] direction. By performing a comprehensive analysis by vector PFM, it was found that the ferroelectric polarization within the domains points in the [1-10] and [00-1] directions, with no indication of an out-of-plane component (see Sec. 3 of the supplementary material for details). The PFM results obtained for the different IDEs are summarized in Fig. 4(b), which gives a schematic illustration of the domain patterns of the (110) BTO film when poled in different in-plane directions. Analogous to Fig. 2(b), the knowledge about the domain structure allows an estimation of the resulting macroscopic polarization, which is expected to be largest for the [1-10]-oriented IDE (blue) and smallest for the [00-1]-oriented IDE (red), consistent with the hysteresis loops shown in Fig. 3(a).

### The (111) oriented BTO film

Ferroelectric hysteresis loops of the (111) BTO film are shown in Fig. 5(a) with the three IDE orientations illustrated in the inset. The ferroelectric hysteresis loops demonstrate a very low anisotropy, consistent with the in-plane sixfold rotational symmetry [see Fig. S1.5(c)]. The corresponding  $\epsilon$ - $E$  loops of the (111) BTO film are displayed in Fig. 5(b), showing nearly isotropic properties. The temperature dependence of the dielectric constant of the (111) BTO film at zero field is shown in Fig. 5(c). The anisotropy in the dielectric constant remained low with the increase in temperature. The Curie temperature for the (111) BTO film was found to be  $155 \pm 5^\circ\text{C}$  for all the three directions. The summary of the observed electrical properties of the (111) BTO film is included in Table I.

The domain structure of the (111) BTO film is shown in the PFM image in Fig. 6(a), which was recorded after poling the film along the [1-10] direction. Different PFM contrast levels (in-plane) and a more complex domain pattern than in the (100) and (110) BTO films are observed. Furthermore, the domain pattern was clearly much more irregular than in (111) BTO bulk samples.<sup>23</sup> In particular, six domain wall orientations were identified.

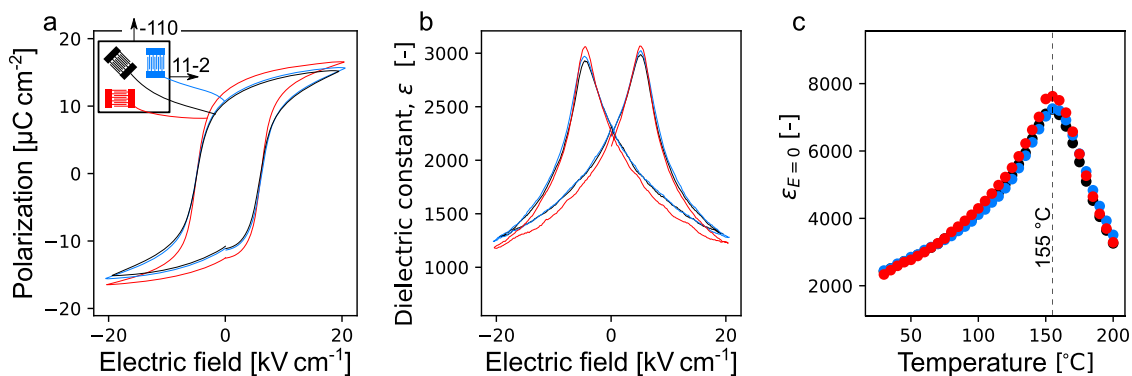


**FIG. 5.** (a) Ferroelectric hysteresis loops (1 Hz) of the (111) BTO film measured with the electric field in the indicated directions on the STO substrate. (b)  $\epsilon$ - $E$  loops of the dielectric constant (1 kHz) for the same orientations. (c) The dielectric constant (1 kHz) of the film as a function of temperature at zero bias field.

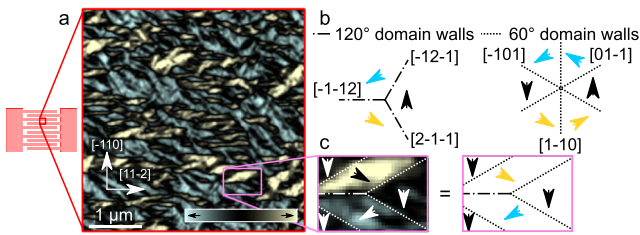


**FIG. 6.** (a) In-plane domain pattern of the poled (111) oriented BTO film between the electrodes oriented with the electric field in the [1-10] direction obtained by phase calibrated PFM. (b) Domain wall configurations separating domains with polarization along the [1-10], [0-11], and [10-1] in-plane directions. Orientation of the polarization in the domains is given by arrows (blue, yellow, and black). 120° and 60° domain walls are shown and labeled according to their orientation on the surface of the film. (c) Magnified image showing 120° and 60° domain walls in the domain pattern.

By using vector PFM, the polarization was observed to manifest along the [1-10], [0-11], and [10-1] in-plane directions, with neutral 120° and 60° domain walls as illustrated in Fig. 6(b). No out-of-plane contrast was observed by vector PFM (see Sec. III of the supplementary material for details). The three different polarization directions were found to intermix in the domain pattern, with both 120° and 60° domain walls present, shown in Fig. 6(c). Importantly, the manifestation of three polarization directions is consistent with the rather isotropic behavior reflected by the hysteresis loops [see Fig. 6(a)].

## DISCUSSION

The BTO films on the three different STO substrates possessed similar thicknesses of about 220 nm, demonstrating a highly robust and reproducible synthesis by aqueous CSD. Increased roughness of (111) BTO films deposited by CSD has previously been observed,<sup>24</sup> but this can be rationalized by the rough surface of the (111) STO substrate (not reported) and the surface energy of (111) BTO, which is higher than (100) and (110) BTO and is therefore energetically unfavorable.<sup>25–27</sup> The three BTO films are highly textured with respect to crystallographic orientation with comparable tensile strain in accordance with the thermal expansion mismatch between the BTO film and the STO substrate.<sup>12</sup> The thermal strain was confirmed to increase the Curie temperature for all three films compared to bulk BTO ( $T_C = 120^\circ\text{C}$ <sup>20</sup>) and the Curie temperature was found to be similar ( $T_C = 155^\circ\text{C}$ ) for all substrate and electrode orientations within the uncertainty ( $\pm 5^\circ\text{C}$ ). The enhanced Curie temperature is in good agreement with the theory of BTO thin films under tensile strain.<sup>4,8,10,11</sup>

The polarization of the films is expected to be low compared to single crystal BTO based on the small difference between the average in-plane and out-of-plane lattice parameters (Table S1.1). Interestingly, the polarization is still higher than what would be expected from the minor difference in the lattice parameters. The ratio between the long and the short axis is only 1.0025 for the (100) BTO film relative to 1.01 for single crystal BTO,<sup>28</sup> and based on this, one could expect a polarization of  $\sim 6 \mu\text{C cm}^{-2}$ . The in-plane ferroelectric and dielectric properties are anisotropic, and the anisotropy

is found to correlate inversely with the in-plane rotational symmetry, where the low (twofold) in-plane rotational symmetry of the (110) orientation yields the large anisotropy, while the high (sixfold) in-plane rotational symmetry of the (111) orientations yields only minor anisotropy (Fig. S1.5). The (110) BTO films are predicted to have in-plane polarization along both the [00-1] and [1-10] in-plane directions, but the predictions do not indicate large anisotropy.<sup>13,14</sup>

The remnant polarization observed correlates inversely with the dielectric constant at zero field, as shown in Fig. S5.1. This follows the trend of tetragonal BTO single crystals, where the dielectric constant has a minimum along the polar axis and a maximum orthogonal to the polar axis.<sup>20</sup> Among the different combinations of electrode and substrate orientations examined here, the (110) oriented BTO film displays both the maximum and minimum values of the in-plane polarization (electric field along [1-10] and [00-1] directions, respectively) and correspondingly also the minimum and maximum dielectric constants at zero field. In general, high polarization also correlates with faster switching dynamics demonstrated by the FWHM of the switching current (Table I). A low FWHM indicates fast switching where the entire film switches in a single event, while a high FWHM indicates a staggered switching process where different regions switch consecutively as the applied voltage is gradually increased. However, not all the data follow these trends. Most notably, for the (100) BTO film, the maximum polarization is found in the same in-plane direction as the maximum in the dielectric constant.

Stable multi-domain structures were observed by PFM for the three orientations. An  $a_1/a_2$  domain pattern was demonstrated for the (100) oriented BTO film, which can explain the anisotropy of the polarization observed for the (100) BTO film. The average domain width is  $55 \pm 19$  nm, which is similar to the previous reports on Landau–Ginzburg–Kittel scaling in unconstrained BTO thin films.<sup>29</sup> The average polarizations along the [010] and [0-11] directions for this domain pattern are illustrated in Fig. 2(b), and the estimated ratio  $P_{010}/P_{0-11}$  based on a theoretical  $a_1/a_2$  domain pattern is  $1/\sqrt{2} \sim 0.71$ , while the results in Table I gives a higher ratio of 0.81. It is, however, clearly demonstrated that the in-plane ferroelectric hysteresis loop is optimized by IDEs oriented parallel to the 90° domain walls in the films, which has not been demonstrated experimentally before. The  $a_1/a_2$  domain pattern also explains why the dielectric constant correlates positively with the remnant polarization.<sup>8</sup> This can be rationalized by considering the fact that the [0-11] in-plane direction only aligns with the average polarization, and not with the local polarization within each domain, yielding a higher dielectric constant than what would otherwise be expected. The relationship between the remnant polarization and dielectric constant has implications for piezoelectric and ferroelectric applications, where a low dielectric constant is generally favorable.

Two types of in-plane domains were also observed for the (110) BTO film, with polarization along the [1-10] and [00-1] axes, respectively, but they are not symmetry equivalent. The domains with polarization along the [1-10] axis have polarization vectors pointing toward an edge of the pseudo-cubic unit cell, similar to orthorhombic BTO, while the [001] domains have polarization pointing toward the facet of the pseudo-cubic unit cell, similar to tetragonal BTO. This is illustrated in Fig. S1.5(b), where the observed polarization

directions are shown as arrows in the pseudo-cubic unit cell. Based on the angle of the domain walls ( $\sim 41^\circ$ ), the polarization is larger in the [1-10] direction than in the [00-1] direction, just as the polarization is larger in orthorhombic BTO than in tetragonal BTO.<sup>28</sup> Furthermore, the volume fraction is skewed in favor of the [1-10] domains. This results in a domain pattern consistent with the hysteresis loops in Fig. 3(a), where larger macroscopic polarization was measured along the [1-10] axis than along the [00-1] axis.

The (111) BTO film was found to have a domain pattern consisting of three types of domains (with  $P \parallel [1-10]$ ,  $[0-11]$ , or  $[10-1]$ ). In all three variants, the polarization points toward an edge in the unit cell and lies in the plane of the film. This is illustrated in Fig. S1.5(c), where the suggested polarization directions are shown using arrows in the pseudo-cubic unit cell. The three types of domains are symmetry equivalent and obey the sixfold rotational symmetry shown in the projection in Fig. S1.5(c). Assuming that the three domain orientations must have equal volume fractions in order to relax the strain, one may calculate the macroscopic polarization along the  $[-110]$  and  $[11-2]$  directions in terms of the polarization in a single domain,  $P_0$ . Using this approach, one finds  $P_{[-110]} = 2/3P_0$  and  $P_{[11-2]} = \sqrt{3}/3P_0$ . This gives a ratio  $P_{[11-2]}/P_{[-110]} = 0.87$ , and a comparable ratio  $P_{[11-2]}/P_{[-110]} = 0.86$  is found using IDEs.

High tunability of the dielectric constant was demonstrated particularly for the (100) and (110) BTO films. Moreover, the tunability was highly sensitive to the in-plane direction of the electric field and reached a maximum for the in-plane direction where the average remnant polarization possessed a minimum. This suggests that the high tunability is related to a rotation of the polarization direction as a bias is applied.<sup>30</sup>

## CONCLUSIONS

In summary, aqueous CSD was used to prepare epitaxial (100), (110), and (111) BTO films on STO substrates. Large variations were demonstrated for both the dielectric and the ferroelectric properties, despite all films having a similar strain state and thickness. In-plane anisotropy was found for all orientations, and the in-plane anisotropy was highest for the orientation with the lowest in-plane rotational symmetry. The polarization and tunability in the dielectric constant were significantly higher for the (110) BTO film compared to the (100) and (111) BTO films, which highlights the importance of considering multiple orientations and crystal anisotropy. Dense domain patterns consisting of multiple domain orientations were observed in all three films, and the domain patterns were consistent with and supported the macroscopic observations. The polarization was found to be inversely correlated with the dielectric constant so that in-plane orientations with a high polarization tended to have a lower dielectric constant. The only exception was the (100) BTO film where the  $a_1/a_2$  domain pattern has a major impact on the properties.

This study has demonstrated that the in-plane ferroelectric and dielectric properties of BTO films under tensile strain can be fine-tuned and optimized by choosing distinct crystallographic orientations. Even for the prototype ferroelectric BTO, this has not been shown for films before. Similar behavior and opportunities for fine-tuning properties in multilayer stacks, where the strain state is given

by the boundary conditions, are anticipated for a range of ferroelectric perovskites, which opens new opportunities for property engineering.

## SUPPLEMENTARY MATERIAL

See the [supplementary material](#) for additional information on (1) x-ray diffraction, (2) transmission electron microscopy, (3) PFM analysis, (4) summary of electrical characterization, (5) dielectric and ferroelectric measurements, (6) dimensions of the interdigitated electrodes, and (7) dielectric constant of the STO substrate.

## ACKNOWLEDGMENTS

The authors thank Donald Evans for fruitful discussions. Financial support of the Norwegian University of Science and Technology (NTNU) and the Research Council of Norway under the Toppforsk program to the project "From Aqueous Solutions to Oxide Thin films and Hierarchical Structures" (Grant No. 250403) and FRIPRO project BORNIT (Grant No. 275139) is gratefully acknowledged. We acknowledge the support of the Research Council of Norway to the Norwegian Micro- and Nano-Fabrication Facility, NorFab (Project No. 245963/F50), and the Norwegian Center for Transmission Electron Microscopy, NORTEM (Project No. 197405/F50). We also acknowledge use of the Norwegian Center for X-ray Diffraction, Scattering and Imaging (RECX).

## DATA AVAILABILITY

The data that support the findings of this study are available from the corresponding author upon reasonable request.

## REFERENCES

- 1D. G. Schlom, L.-Q. Chen, C.-B. Eom, K. M. Rabe, S. K. Streiffer, and J.-M. Triscone, *Annu. Rev. Mater. Res.* **37**, 589 (2007).
- 2A. R. Damodaran, J. C. Agar, S. Pandya, Z. Chen, L. Dedon, R. Xu, B. Apgar, S. Saremi, and L. W. Martin, *J. Phys.: Condens. Matter* **28**, 263001 (2016).
- 3D. G. Schlom, L.-Q. Chen, C. J. Fennie, V. Gopalan, D. A. Muller, X. Pan, R. Ramesh, and R. Uecker, *MRS Bull.* **39**, 118 (2014).
- 4K. J. Choi, *Science* **306**, 1005 (2004).
- 5J. H. Haeni, P. Irvin, W. Chang, R. Uecker, P. Reiche, Y. L. Li, S. Choudhury, W. Tian, M. E. Hawley, B. Craigo, A. K. Tagantsev, X. Q. Pan, S. K. Streiffer, L. Q. Chen, S. W. Kirchoefer, J. Levy, and D. G. Schlom, *Nature* **430**, 758 (2004).
- 6N. A. Pertsev, A. K. Tagantsev, and N. Setter, *Phys. Rev. B* **65**, 219901 (2002).
- 7N. A. Pertsev, A. G. Zembilgotov, and A. K. Tagantsev, *Phys. Rev. Lett.* **80**, 1988 (1998).
- 8R. Waser, N. A. Pertsev, and V. G. Koukhar, *Phys. Rev. B* **64**, 214103 (2001).
- 9O. Diéguez, S. Tinte, A. Antons, C. Bungaro, J. B. Neaton, K. M. Rabe, and D. Vanderbilt, *Phys. Rev. B* **69**, 212101 (2004).
- 10Y. L. Li and L. Q. Chen, *Appl. Phys. Lett.* **88**, 072905 (2006).
- 11A. Grünebohm, M. Marathe, and C. Ederer, *Appl. Phys. Lett.* **107**, 102901 (2015).
- 12T. M. Raeder, K. Bakken, J. Glaum, M. A. Einarsrud, and T. Grande, *AIP Adv.* **8**, 105228 (2018).
- 13Z. Gui, S. Prosandeev, and L. Bellaiche, *Phys. Rev. B* **84**, 214112 (2011).
- 14H. Wu, X. Ma, Z. Zhang, J. Zeng, J. Wang, and G. Chai, *AIP Adv.* **6**, 015309 (2016).
- 15C. H. Nguyen, R. Nigon, T. M. Raeder, U. Hanke, E. Halvorsen, and P. Murali, *J. Phys. D.* **51**, 175303 (2018).



- <sup>16</sup>T. M. Ræder, E. Halvorsen, U. Hanke, and T. Grande, *Smart Mater. Struct.* **29**, 115039 (2020).
- <sup>17</sup>T. Suzuki, Y. Nishi, and M. Fujimoto, *Philos. Mag. A* **79**, 2461–2483 (1999).
- <sup>18</sup>M. Tyunina, O. Pacherova, J. Peräntie, M. Savinov, M. Jelinek, H. Jantunen, and A. Dejneka, *Sci. Rep.* **9**, 3677 (2019).
- <sup>19</sup>C. B. Carter and M. G. Norton, *Ceramic Materials: Science and Engineering* (Springer, 2007).
- <sup>20</sup>W. J. Merz, *Phys. Rev.* **75**, 687 (1949).
- <sup>21</sup>D. L. Kaiser, M. D. Vaudin, L. D. Rotter, Z. L. Wang, J. P. Cline, C. S. Hwang, R. B. Marinenko, and J. G. Gillen, *Appl. Phys. Lett.* **66**, 2801 (1995).
- <sup>22</sup>A. S. Everhardt, S. Matzen, N. Domingo, G. Catalan, and B. Noheda, *Adv. Electron. Mater.* **2**, 1500214 (2016).
- <sup>23</sup>P. S. Bednyakov, T. Sluka, A. K. Tagantsev, D. Damjanovic, and N. Setter, *Sci. Rep.* **5**, 11 (2015).
- <sup>24</sup>T. Hosokura, A. Ando, and T. Konoike, *RSC Adv.* **5**, 97563 (2015).
- <sup>25</sup>M. Nakayama, S. Hotta, T. Nakamura, and T. Kasuga, *J. Ceram. Soc. Jpn.* **121**, 611 (2013).
- <sup>26</sup>R. I. Eglitis, *Appl. Surf. Sci.* **358**, 556 (2015).
- <sup>27</sup>R. Eglitis, J. Purans, A. I. Popov, and R. Jia, *Int. J. Mod. Phys. B* **33**, 1 (2019).
- <sup>28</sup>H. F. Kay and P. Vousden, *Philos. Mag.* **40**, 1019 (1949).
- <sup>29</sup>I. A. Luk'yanchuk, A. Schilling, J. M. Gregg, G. Catalan, and J. F. Scott, *Phys. Rev. B* **79**, 144111 (2009).
- <sup>30</sup>M. Davis, M. Budimir, D. Damjanovic, and N. Setter, *J. Appl. Phys.* **101**, 054112 (2007).